J. Fluid Mech. (2018), *vol.* 835, *pp.* 24–44. © Cambridge University Press 2017
doi:10.1017/jfm.2017.755

Non-isolated drop impact on surfaces

Y. Wang[1] **and L. Bourouiba**[1,†]

[1]The Fluid Dynamics of Disease Transmission Laboratory, Massachusetts Institute of Technology, Cambridge, MA 02139, USA

(Received 20 February 2017; revised 4 October 2017; accepted 13 October 2017; first published online 27 November 2017)

Upon impact on a solid surface, a drop expands into a sheet, a corona, which can rebound, stick or splash and fragment into secondary droplets. Previously, focus has been placed on impacts of single drops on surfaces to understand their splash, rebound or spreading. This is important for spraying, printing, and environmental and health processes such as contamination by pathogen-bearing droplets. However, sessile drops are ubiquitous on most surfaces and their interaction with the impacting drop is largely unknown. We report on the regimes of interactions between an impacting drop and a sessile drop. Combining experiments and theory, we derive the existence conditions for the four regimes of drop–drop interaction identified, and report that a subtle combination of geometry and momentum transfer determines a critical impact force governing their physics. *Crescent-moon* fragmentation is most efficient at producing and projecting secondary droplets, even when the impacting drop Weber number would not allow for splash to occur on the surface considered if the drop were isolated. We introduce a critical horizontal impact Weber number We_c that governs the formation of a sheet from the sessile drop upon collision with the expanding corona of the impacting drop. We also predict and validate important properties of the crescent-moon fragmentation: the extension of its sheet base and the ligaments surrounding its base. Finally, our results suggest a new paradigm: impacts on most surfaces can make a splash of a new kind – a crescent-moon – for any impact velocity when neighbouring sessile drops are present.

Key words: aerosols/atomization, drops, drops and bubbles

1. Introduction and observations: ubiquity of non-isolated impacts

The outcome of the impact of a drop depends on its impacting energy and the surface wetting properties. Upon impact on a solid surface, a drop expands into a sheet, a corona, which can rebound, stick or splash and fragment into secondary droplets (Rioboo, Marengo & Tropea 2002; Yarin 2006). Numerous studies have focused on impacts of single drops on superhydrophobic surfaces to understand when and how splash, rebound or coating occurs. This is important for spray-coating, deicing, pesticide spraying (Zable 1977; Eggers & Villermaux 2008; Josserand & Thoroddsen 2016), and for environmental and health processes such as erosion (Furbish *et al.* 2007) or contaminant dissemination by secondary pathogen-bearing

† Email address for correspondence: lbouro@mit.edu

droplets (Bourouiba & Bush 2013; Bourouiba, Dehandschoewercker & Bush 2014; Gilet & Bourouiba 2014, 2015; Scharfman *et al.* 2016). However, most natural and indoor surfaces have average-wetting – neither superhydrophobic nor superhydrophilic – properties and support sessile drops. The physics of a single drop impact on most surfaces can be dramatically changed by the presence of adjacent sessile drops (Sivakumar & Tropea 2002; Moreira, Moita & Panão 2010; Gilet & Bourouiba 2014; Liang & Mudawar 2016). Yet, little attention has been paid to interactions between impacting drops and sessile drops surrounding them on average-wetting surfaces (Charalampous & Hardalupas 2016). Instead, the focus has been on the impact of isolated drops on surfaces, predicting, for example, the maximum radius of expansion of the corona they form upon impact, r_{max}, and the number of corrugations, N, that appear on the rim surrounding such expanding corona. Here, we focus on the neglected case of drop impact on surfaces of average wetting that hold sessile drops.

1.1. *Types of drop–drop impact*

Two types of impact on a leaf supporting a sessile drop are illustrated experimentally in figure 1(*a*,*b*). A rain or irrigation spray drop, of radius r_1, can either impact a sessile drop of radius r_2 *head-on*, at its centre (figure 1*a*), or off-centre, leading to a *crescent-moon* fragmentation (figure 1*b*). When off-centre, with an interdrop distance d, the impacting drop viewed from the bottom (figure 2*c*) spreads into a circular corona which collides with the sessile drop (figures 1*b*, 2*c*). Viewed from the side, the collision results in lift of the sessile drop from the surface to form an arched sheet (figures 1*b*, 2*b*) expanding in the air with a profile shaped as a crescent-moon (figure 2*a*), which eventually fragments into droplets. Viewed from below, quickly following the lift of the sessile drop, two filaments emerge at the edge of the foot of the crescent-moon sheet and grow (figures 1*a* and 2*c*). A few studies have reported the interaction of coronas (Barnes *et al.* 1999) or head-on collisions of trains of drops on surfaces (Yarin & Weiss 1995; Fujimoto, Ito & Takezaki 2002).

However, the probability of an off-centre impact such as in figure 2(*a–c*) is much higher than that of a head-on impact. Hence, crescent-moon fragmentation is a more frequent and efficient source of secondary droplets in spray- or rain-induced foliar disease transmission (Gilet & Bourouiba 2015). Indeed, common leaves have average wetting – neither superhydrophobic nor superhydrophilic – and support sessile drops (Gilet & Bourouiba 2014). The physics of the crescent-moon generalizes beyond impacts on leaves and provides an explanation of difficulties in achieving uniform coatings or suppressing undesired secondary droplet ejection from most common surfaces of average wetting (figure 2*a*). Even when the impacting drop is below the splash limit, the presence of a sessile drop in the vicinity can still generate undesired ejection of secondary droplets (figure 2*a–c*), thus making it important to gain an understanding of this recently discovered phenomenon. Before discussing our observations further, we start by reviewing the body of literature on isolated drop impact on surfaces, with a particular focus on the maximum corona radius r_{max} they reach, and the number of corrugations N observed on the rim of their corona.

1.2. *Maximum corona radius and corrugations: prior literature results*

We consider the impact of an isolated drop of radius r_1 with normal impact Weber number $We = \rho u_1^2(2r_1)/\sigma$, where r_1 is the radius of the impacting drop, u_1 is the impact speed, and ρ, ν and σ are the density, kinematic viscosity and surface tension of the drop respectively. Upon impact, the drop expands in the form of a

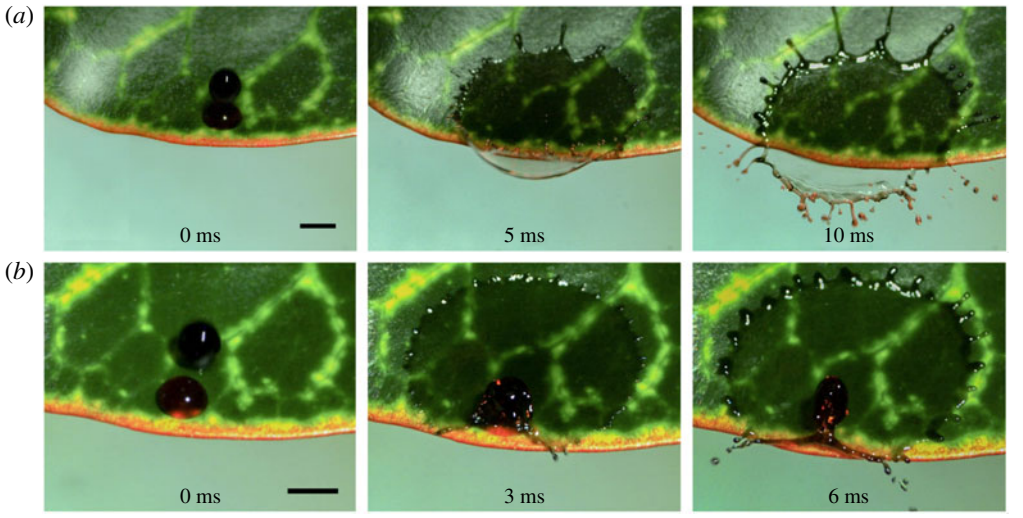

FIGURE 1. (Colour online) Drop–drop interactions on a leaf. (*a*) A drop hits a sessile drop right at its centre, forming a head-on collision. (*b*) A drop hits a sessile drop off-centre, leading to a crescent-moon with universal sheet lift and growth of a pair of bounding ligaments. The scale bar is 5 mm.

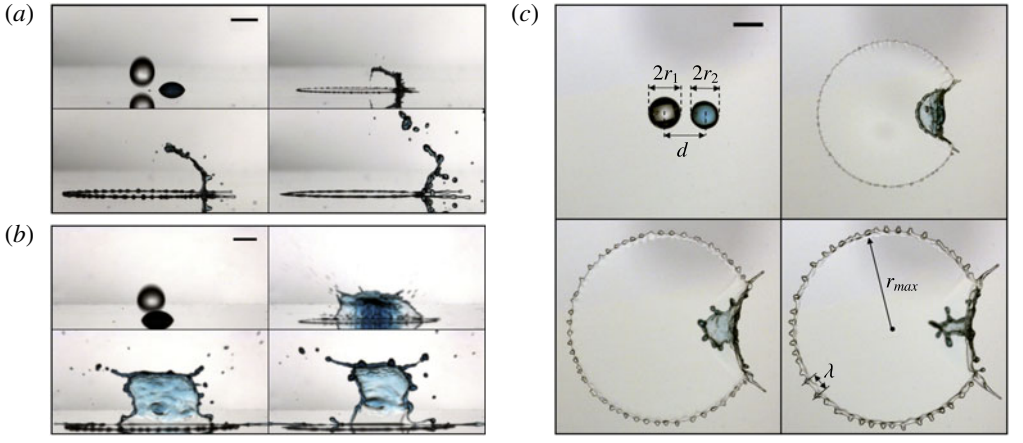

FIGURE 2. (Colour online) Crescent-moon formation. (*a*) From impacting clear drop, to lift of the blue sessile drop, to its stretching and onset of fragmentation. Both drops are made of water with density $\rho = 1.0 \times 10^3$ kg m^{-3}, viscosity $\nu = 1.0 \times 10^{-6}$ m^2 s^{-1} and surface tension $\sigma = 72$ mNm^{-1}. The radii are $r_1 = 2.24$ mm and $r_2 = 1.95$ mm for the impacting and sessile drop respectively. (*b*) Side view of the crescent-moon formation shown in (*a*), displaying the stretching of the sessile drop into an arched sheet as it lifts from the surface. (*c*) Bottom view of the expanding corona of the impacting drop lifting the sessile drop, at distance $d = 5.65$ mm from impact, and emergence of the pair of ligaments bounding the base of the crescent-moon sheet. Here, r_{max} is the maximum radius of the corona and λ is the average wavelength (distance) between rim corrugations at the maximum radius. The time interval is 0.12 ms and the scale bar is 5 mm.

corona which reaches a maximum radius r_{max} (figure 2*c*). Two particular regimes of such corona spreading have been predominantly discussed in the literature (table 1): a viscous dominated regime and a capillary dominated regime. In the capillary dominated regime, viscous effects are neglected. In this first regime, lossless conversion of the impacting drop kinetic energy to the corona surface energy is assumed to set r_{max}, leading to $R_{max} = r_{max}/r_1 \sim We^{1/2}$ first derived by Madejski (1976). Lastakowski *et al.* (2014) more recently reported $R_{max} \sim We^{1/2}$ based on experiments on superheated surfaces which reduce viscous stresses. Clanet *et al.* (2004) proposed a scaling $R_{max} \sim We^{1/4}$ on superhydrophobic surfaces based on mass conservation and considering an average corona thickness $h = \sqrt{\sigma/\rho a}$, with $a = u_1^2/d_1$ the impact acceleration and d_1 the impacting drop diameter. The R_{max} observed in their experiments was smaller than their prediction. These authors conjectured that the missing energy was converted to internal circulation in the corona. In the viscous regime, surface tension is neglected. In this second regime, Madejski (1976) and Chandra & Avedisian (1991) predicted $R_{max} \sim Re^{1/5}$ by considering full viscous dissipation of the impacting drop kinetic energy, where $Re = (2r_1)u_1/\nu$ is the Reynolds number and ν is the kinematic viscosity of the fluid. This scaling is also consistent with the experimental data reported by Clanet *et al.* (2004).

Eggers *et al.* (2010) attempted to combine the viscous and capillary dominated regimes and proposed a unified expression $R_{max} = Re^{1/5} f(P)$, with $P = We\, Re^{-2/5}$ when energy conservation holds as in Madejski (1976) or $P = We\, Re^{-4/5}$ when impact inertia is dominant as in Clanet *et al.* (2004). More recently, Laan *et al.* (2014) collapsed all of the experimental data available on R_{max} from both the viscous and capillary dominated regimes and also proposed a unified scaling as

$$R_{max} = Re^{1/5} f(P), \quad \text{with } P = We\, Re^{-2/5}, \tag{1.1}$$

where the empirical expression of $f(P)$ was proposed using the Padé approximant,

$$f_c(P) = \frac{P^{1/2}}{A + P^{1/2}}, \tag{1.2}$$

with fitting parameter $A = 1.24 \pm 0.02$. Lee *et al.* (2016) extended the Padé approximant of Laan *et al.* (2014) by incorporating surface wetting via a contact angle θ_e, leading to $\tilde{R}_{max} = (R_{max}^2 - R_{v\to 0}^2)^{1/2}$, where $R_{v\to 0}$ is the drop dimensionless radius when deposited (without inertia) on the surface,

$$\tilde{R}_{max} = f_c(We) = \frac{We^{1/2}}{B + We^{1/2}}, \tag{1.3}$$

with fitting parameter $B = 7.6$.

Scheller & Bousfield (1995) considered drop impacts on a range of materials from glass to plastic and for the widest range of Weber number from 50 to 2500. The initial fit to their data for maximum radius led to

$$R_{max} = 0.61(Re^2 Oh)^{1/6} = 0.61\, Re^{1/5}(We\, Re^{-2/5})^{1/6}, \tag{1.4}$$

which can also be expressed as $R_{max} = Re^{1/5} f(P)$ in the form proposed by Eggers *et al.* (2010). Scheller & Bousfield (1995) also discussed a prediction of R_{max} based on a 'squeeze flow model', assuming that the impacting drop squeezes in the form of a cylindrical column. This geometry, combined with conservation of mass and

https://doi.org/10.1017/jfm.2017.755 Published online by Cambridge University Press

Study	R_{max}	Liquid	Surface	We	Re
Madejski (1976)	$\sim We^{1/2}$ $\sim Re^{1/5}$	Lead and tin	Wood, plexiglas, metal	>100 ∞	∞ >100
Scheller & Bousfield (1995)	$=0.61\,(Re^2 Oh)^{1/6}$ $=0.61\,Re^{1/5}(We\,Re^{-2/5})^{1/6}$	Glycerol–water–ethanol mixture	Plastic and glass	50–2500	20–16 400
Clanet *et al.* (2004)	$\sim We^{1/4}$	Water, mercury	Superhydrophobic	2–900	$We\,Re^{-4/5}<1$
Eggers *et al.* (2010)	$=Re^{1/5} f(We\,Re^{-2/5})$	Simulation		400–16 000	800–8000
Laan *et al.* (2014)	$=Re^{1/5}\dfrac{P^{1/2}}{1.24+P^{1/2}}$, with $P=We\,Re^{-2/5}$	Glycerol–water mixture	Stainless steel	10–1700	70–17 000
Lee *et al.* (2016)	$\tilde{R}_{max}=Re^{1/5}\dfrac{We^{1/2}}{7.6+We^{1/2}}$ with $\tilde{R}_{max}=(R_{max}^2-R_{v\to 0}^2)^{1/2}$	Ethanol, water, glycerol	Glass, steel, parafilm	1–1500	40–18 000

TABLE 1. Summary of scaling laws proposed in prior work for the maximum spreading of isolated impacting drops on surfaces, $R_{max}=r_{max}/r_1$, where r_1 is the impacting drop radius.

Study	N	Liquid	Surface	We	Re
Marmanis & Thoroddsen (1996)	$\sim(Re^{1/2}\,We^{1/4})^{3/4} = \left(\frac{We}{Oh}\right)^{3/8}$	Water	Stiff paper	100–4000	1100–25 000
Bhola & Chandra (1999)	$\sim Re^{1/4}\,We^{1/2} = \frac{We^{5/8}}{Oh^{1/4}}$	Paraffin wax	Aluminium	25–750	200–1150
Mehdizadeh, Chandra & Mostaghimi (2004)	$\sim We^{1/2}$	Water	Stainless steel	100–50 000	5500–65 000

TABLE 2. Summary of literature scaling laws proposed to quantify the number of rim corrugations, N, surrounding the corona of a single impacting drop.

momentum, and considering viscous stress and surface tension as external forces, leads to

$$R_{max} = (Re^2 Oh)^{0.123}, \tag{1.5}$$

which is close to the best fit of their experimental data (1.4). In summary, we can re-express (1.1), (1.3) and (1.4) as

$$R_{max} = \frac{We^{1/2}}{1.24 + We^{2/5}Oh^{1/5}}, \quad \tilde{R}_{max} = \frac{We^{2/5}Oh^{-1/5}}{7.6 + We^{1/2}}, \quad R_{max} = 0.61\left(\frac{We}{Oh}\right)^{1/6} \tag{1.6a–c}$$

respectively. These expressions are summarized with additional details in table 1.

In the literature, the number of corrugations, N, at maximum corona radius r_{max} was linked to the destabilization wavelength of the rim, $N = 2\pi r_{max}/\lambda$ (see figure 2*c* for illustration of λ). A summary of prior literature predictions of N is given in table 2. In particular, Marmanis & Thoroddsen (1996) first conducted an experimental study of the corrugations for drop impacts on paper and found N to scale with the 'impact Reynolds number' $Re_I = u_1\delta/\nu$, where $\delta = \sqrt{\nu\tau_c}$ is the boundary layer thickness based on the drop free oscillation period, essentially the capillary timescale $\tau_c = \sqrt{\rho 8r_1^3/\sigma}$, yielding

$$N = B(Re_I)^{3/4} = B(Re^{1/2}We^{1/4})^{3/4} = B\left(\frac{We}{Oh}\right)^{3/8}, \tag{1.7}$$

where the coefficient B was not explicitly given by the authors.

Bhola & Chandra (1999) estimated $N = 2\pi r_{max}/\lambda$, with $r_{max}/r_1 \sim Re^{1/4}$ proposed in their study, with $\lambda = 2\pi\sqrt{3\sigma/a\rho}$ the wavelength characteristic of the Rayleigh–Taylor instability with a characteristic acceleration $a = u_1^2/2r_1$, leading to

$$N = \frac{Re^{1/4}We^{1/2}}{4\sqrt{3}} = \frac{We^{5/8}}{4\sqrt{3}\,Oh^{1/4}}. \tag{1.8}$$

Mehdizadeh *et al.* (2004) conducted a theoretical study of the temporal evolution of the corrugations by considering small initial perturbations of the corona rim and using a linear Rayleigh instability analysis. They inferred a decreasing value of N with corona expansion, but did not express N at maximum corona radius explicitly.

In this study, combining experiments and theory, we show that an impacting drop that would not splash in isolation, but coat the surface, can still lead to secondary

r_1 (mm)	r_2 (mm)	d (mm)	u_1 (m s^{-1})	We	Re ($\times 10^4$)	Oh ($\times 10^{-3}$)	No. of exp.
	$1.12 \sim 3.36$	$0.4 \sim 10.3$	2.31 ± 0.04	371 ± 3	1.13 ± 0.01		31
	$1.10 \sim 2.88$	2.5–12.5	3.35 ± 0.04	778 ± 4	1.61 ± 0.04		31
2.36 ± 0.06	1.22–2.86	1.2–14.5	4.24 ± 0.03	1226 ± 8	1.95 ± 0.07	1.75 ± 0.04	52
	1.34–3.30	1.7–17.8	5.28 ± 0.06	1926 ± 28	2.48 ± 0.08		53
	1.23–3.10	0.4–18.0	5.91 ± 0.08	2405 ± 30	2.81 ± 0.09		57

TABLE 3. The experimental conditions for the water drop–drop impact experiments. Deionized water was used for both the falling drops and the sessile drops with density, kinematic viscosity and surface tension $\rho = 1.0 \times 10^3$ kg m^{-3}, $\nu = 1.0 \times 10^{-6}$ m^2 s^{-1} and $\sigma = 72$ mN m^{-1} respectively. The Weber number $We = \rho u_1^2 (2r_1)/\sigma$, Reynolds number $Re = (2r_1)u_1/\nu$ and Ohnesorge number $Oh = \mu/\sqrt{\rho\sigma(2r_1)}$ involved are also given. The averaged wetting of the surface used was similar to that of plant leaves supporting crescent-moon fragmentation (figure 1).

droplets in the presence of a sessile drop. Our focus is on the impact of rain or irrigation drops on intermediate-wetting surfaces supporting sessile contaminated drops with potential for secondary contaminated drop ejection. We revisit the predictions of maximum corona radius R_{max} and corrugations N for impacts on average-wetting surfaces. We identify four regimes of drop–drop interaction: *head-on collision*, *crescent-moon fragmentation*, *touch-and-flop collision* and *no collision* (§ 2). We combine experiments and theory to derive the conditions under which these regimes occur, and find that a subtle combination of geometry and momentum transfer determines a critical drop–drop impact force governing the existence and inter-regime boundaries and the physics of the crescent-moon new splash phenomenon (§ 3). We introduce a horizontal critical collision Weber number We_c which determines when crescent-moon fragmentation can occur. The critical collision Weber number We_c is defined based on the force per unit length upon collision of the corona rim on the sessile drop (§§ 3.3.1–3.3.2). Finally, we also predict key properties of the crescent-moon fragmentation: the extension of its base (§ 4) and the length of the pair of ligaments always surrounding its base (§ 5). These properties are important for study of the highly efficient fragmentation process that is the crescent-moon (§ 6).

2. Experimental set-up and observations: regimes of drop–drop interaction

We conducted systematic collision experiments involving a water drop impacting in the vicinity of sessile drops of increasing viscosity (from water to pure glycerol), with properties summarized in tables 3 and 4. The impacts were recorded by two high-speed cameras from side and bottom views (figures 4 and 2). An impacting drop of radius r_1 was released from a height of 0.3–2.2 m onto an impact point at distance d from the centre of a sessile drop of radius r_2 (table 3). The sessile drop was deposited on surfaces of average wetting with static equilibrium contact angles $45^\circ \leqslant \theta_E \leqslant 82^\circ$. Upon expansion of the impacting drop, the expanding corona grows and reaches a maximum radius r_{max} (figure 2*c*). For every impacting drop speed u_1 and size r_1, the distance d between the impact point and the centre of the sessile drop and the size of the sessile drop r_2 were varied. Our large set of experiments allowed us to identify four drop–drop interaction regimes: *head-on collision*, *crescent-moon fragmentation*, *touch-and-flop collision* and *no collision* (figure 3*a–h*).

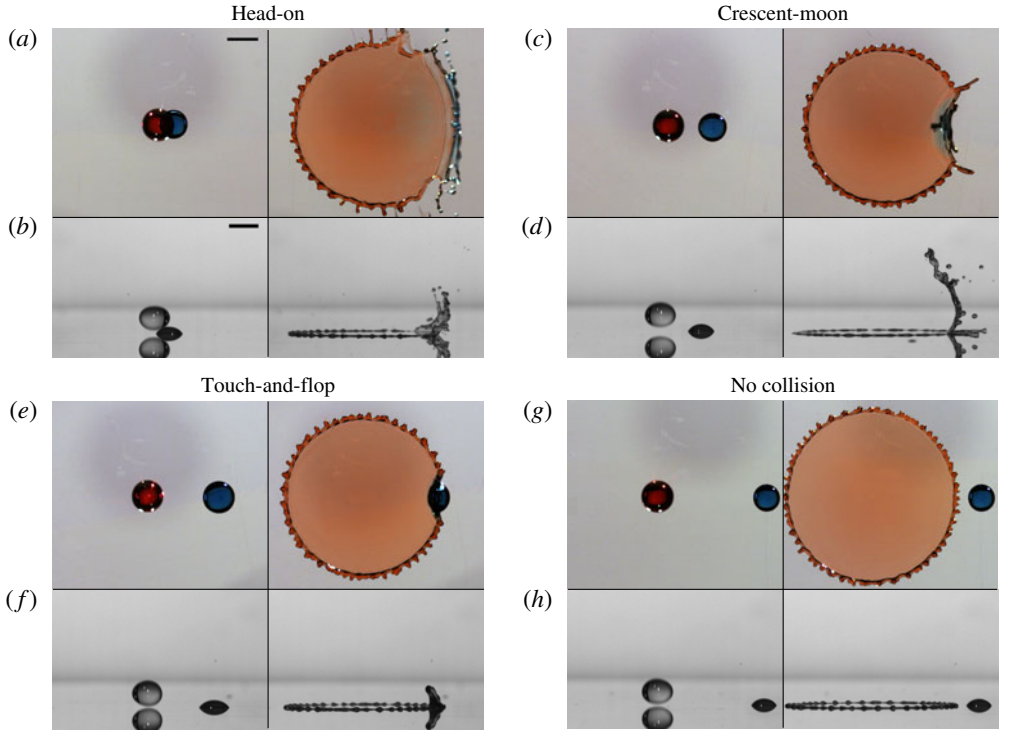

FIGURE 3. (Colour online) The four possible scenarios of drop–drop interaction. In each quadrant, the upper two panels are imaged from below, while the lower panels are imaged simultaneously from the side. The red impacting drop radius is $r_1 = 2.27$, 2.29, 2.31, 2.31 mm for (*a*), (*c*), (*e*), (*g*) respectively. The blue sessile drop radius is $r_2 = 2.29$, 2.24, 2.60, 2.16 mm for (*a*), (*c*), (*e*), (*g*) respectively. The drop–drop distance is $d = 2.51$, 6.85, 11.51, 17.68 mm for (*a*), (*c*), (*e*), (*g*) respectively.

r_1 (mm)	r_2 (mm)	d (mm)	u_1 (m s^{-1})	Material of sessile drops	Density ρ ($\times 10^3$ kg m^{-3})	Viscosity ν ($\times 10^{-3}$ m^2 s^{-1})	No. of exp.
	1.63–3.22	6.1–13.1		Water	1.000	0.001	20
	1.55–2.53	6.1–12.2		Mixture 1	1.131	0.008	15
2.33 ± 0.04	1.58–3.26	4.6–12.4	4.06 ± 0.06	Mixture 2	1.175	0.027	15
	1.94–2.61	4.8–10.7		Glycerol	1.264	1.414	10
	2.51–3.95	6.7–14.5		Plastic (solid)	1.2	∞	10

TABLE 4. The experimental parameters used for drop–drop collisions with sessile drops of increasing viscosity and with a solid drop-analogue. Mixture 1 is made of a 1 : 1 volume ratio of water to glycerol. Mixture 2 has a 1 : 2 volume ratio. The density, kinematic viscosity and surface tension of the falling drops are the same as those given in table 3, with corresponding $We = 1063 \pm 26$, $Re = (1.89 \pm 0.04) \times 10^4$ and $Oh = (1.73 \pm 0.03) \times 10^{-3}$.

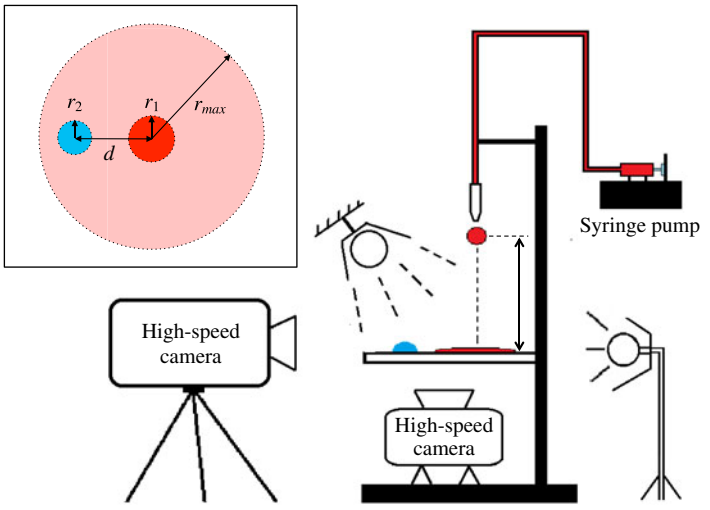

FIGURE 4. (Colour online) Schematic of the experimental set-up. The inset shows the scheme of the impact phenomenon viewed from the top. The red circle indicates the impacting drop and the blue circle the sessile drop. The radii of the impacting drop and the sessile drop are r_1 and r_2 respectively. The centre-to-centre offset between the sessile drop and the impact point is d; r_{max} is the maximum radius of the expanding corona.

3. Boundary between the regimes of drop–drop interaction

3.1. *Head-on collision*

We capture the transition between the four regimes (figure 3) with only two parameters: the impact Weber number $We = \rho u_1^2(2r_1)/\sigma$ and the dimensionless drop–drop distance $D = (d - r_2)/r_1$. If the impacting drop contacts the sessile drop prior to touch-down on the surface, then a head-on drop–drop interaction occurs (figures 1*a* and 3*a*,*b*). This regime emerges for drop–drop offsets d that are smaller than the sum of the radii of the two drops, namely for

$$d < r_1 + r_2 \quad \text{or} \quad D < 1. \tag{3.1a,b}$$

Depending on the relative drop sizes, the impact is analogous to (i) an isolated drop impact on a surface, where the expanding corona of the impacting drop seamlessly swallows the sessile drop ($r_1/r_2 \gg 1$), (ii) an impact on thin film ($r_1/r_2 \ll 1$) or (iii) an asymmetric non-isolated drop impact on a solid surface ($r_1/r_2 \sim O(1)$), as seen in figures 1(*b*) and 3(*a*,*b*).

3.2. *No collision and maximum corona radius*

If the impacting drop corona is smaller than the drop–drop distance, no collision occurs, making this an isolated drop impact. This scenario (figure 3*g*,*h*) is captured by

$$d > r_{max} + r_2 \quad \text{or} \quad D > \frac{r_{max}}{r_1} = R_{max}, \tag{3.2a,b}$$

where R_{max} is the dimensionless spreading of the impacting drop. A number of prior studies have examined isolated drop impacts on solid surfaces and aimed to

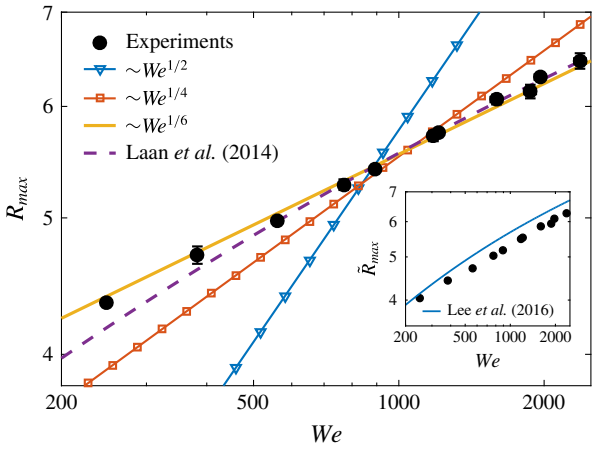

FIGURE 5. (Colour online) Comparison of our measured isolated drop $R_{max} = r_{max}/r_1$ as a function of impact Weber number We (black dots) with literature predictions summarized in table 1. Our data, obtained with the conditions summarized in table 5, are best captured by $R_{max} = 0.61(We/Oh)^{1/6}$ from Scheller & Bousfield (1995). Here, the Weber number $We = \rho u_1^2(2r_1)/\sigma$ and the Ohnesorge number $Oh = \mu/\sqrt{\rho\sigma(2r_1)}$.

r_1 (mm)	u_1 (m s^{-1})	We	Re ($\times 10^4$)	Oh ($\times 10^{-3}$)	No. of exp.
	1.96 ± 0.01	245 ± 2	0.89 ± 0.01		15
	2.54 ± 0.02	409 ± 1	1.16 ± 0.02		15
	2.93 ± 0.03	549 ± 8	1.35 ± 0.05		15
2.29 ± 0.01	3.72 ± 0.04	884 ± 7	1.71 ± 0.07	1.74 ± 0.01	15
	4.42 ± 0.02	1250 ± 5	2.03 ± 0.01		15
	5.03 ± 0.05	1607 ± 30	2.30 ± 0.03		15
	5.53 ± 0.08	1978 ± 44	2.55 ± 0.04		15

TABLE 5. Experimental conditions and number of experiments in the present study used to quantify the maximum radius $R_{max} = r_{max}/r_1$ (§ 3.2) and the number of ligaments N (figure 9) of the impacting drop expanding corona. Given our focus on the impact of rain and irrigation drops, the density, kinematic viscosity and surface tension of the impacting drops are those of water: $\rho = 1.0 \times 10^3$ kg m^{-3}, $\nu = 1.0 \times 10^{-6}$ m^2 s^{-1} and $\sigma = 72$ mN m^{-1} respectively.

express $R_{max} = r_{max}/r_1$ as a function of the impact Weber and Reynolds numbers, $We = \rho u_1^2(2r_1)/\sigma$ and $Re = (2r_1)u_1/\nu$ respectively (table 1 and § 1.2).

Given the disparities in prior literature predictions of maximum corona radius for a range of eclectic surfaces and fluids, and our focus on impacts of water drops on surfaces of average wetting relevant for irrigation or washing of crop and fresh produce, we proceed to conduct more than a hundred isolated water drop impact experiments to determine the relevant maximum radius on our surfaces (table 5). The impacting drop viscosity μ, surface tension σ and size r_1 are such that $Oh = (1.74 \pm 0.01) \times 10^{-3}$ is fixed, while We ranges from 240 to 2020 (see table 5 for the full list of parameters).

Figure 5 shows our experimental measurements of maximum corona radius R_{max} as a function of drop impact We. When compared with the literature (table 1), our

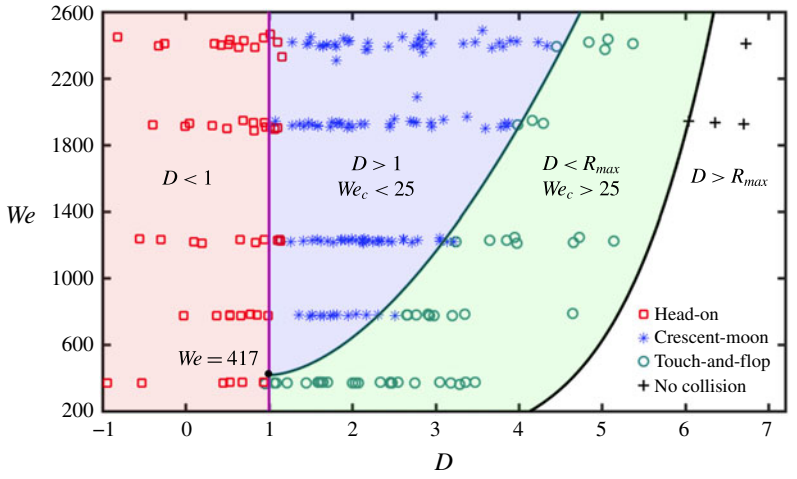

FIGURE 6. (Colour online) Regime map of the outcome of drop–drop interaction as a function of $D = (d - r_2)/r_1$, $R_{max} = r_{max}/r_1$ and $We = \rho u_1^2(2r_1)/\sigma$. The collision threshold Weber number $We_c = 25$ derived in the text is used to analytically derive the boundaries between the regimes. All experimental values are found in tables 3–5. The boundaries between the regimes are elucidated and derived one by one in § 3.

results are consistent with the scaling of Scheller & Bousfield (1995) and Laan *et al.* (2014), and are best captured by $R_{max} \sim We^{1/6}$ from Scheller & Bousfield (1995), who conducted experiments over an analogous range of impact *We* and *Re* to our study (tables 1 and 5). From figure 5, we obtain

$$R_{max} = \frac{r_{max}}{r_1} = C_R\, We^{1/6}, \tag{3.3}$$

with $C_R = 0.61/Oh^{1/6} = 1.75$ given (1.6) and $Oh = 1.75 \times 10^{-3}$, which is fixed here (table 3). The experiments presented in this section allow us to fix the expression for R_{max} as (3.3) with $C_R = 1.75$ for the remainder of this study.

3.3. *Boundary between crescent-moon and touch-and-flop collision*

Crescent-moon fragmentation and touch-and-flop collision can only exist for $1 < D < R_{max}$. Crescent-moon fragmentation occurs if the sessile drop is lifted and transformed into an expanding arched sheet, ultimately fragmenting into secondary droplets (figures 2*a–c*, 3*c*,*d*). The onset of the touch-and-flop collision is similar to that of the crescent-moon, with an initial lift of the sessile drop; however, the sessile drop remains a coherent bulk without topological change into a thin sheet. This results in the sessile fluid being simply displaced to form another sessile drop in the vicinity of the original one (figure 3*e*,*f*). We summarize in figure 6 our results and prediction of transition criteria between drop–drop interaction regimes in a phase diagram of *We* versus *D*.

3.3.1. *Physical picture and threshold impact force*

To understand the more subtle transition between the crescent-moon and the touch-and-flop collision, we consider the following. Upon impact with a given *We*,

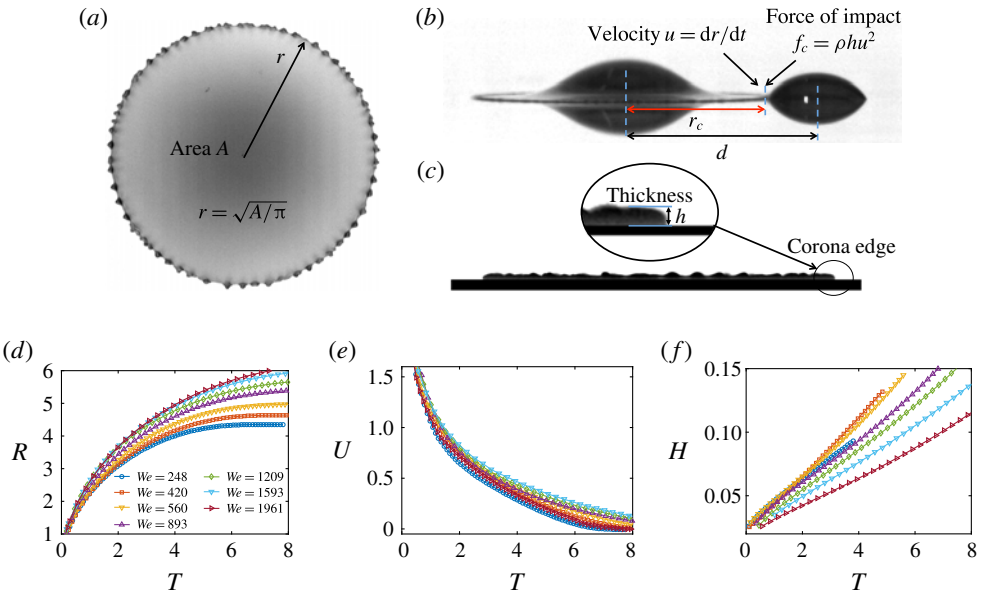

FIGURE 7. (Colour online) (*a*) Top view of the expanding corona, the contour of which is detected using image processing, allowing us to deduce a radial expansion velocity $u = \mathrm{d}r/\mathrm{d}t$, where r is the radius of the corona. This radius was determined by measurement of the temporal evolution of the corona area A and $r = \sqrt{A/\pi}$. (*b*) The side view allows us to measure the radius of the corona at the time of collision with the sessile drop, r_c, and to track the evolution of the thickness of the corona edge h (*c*). These side and top views allow us to define a force of impact per unit arclength of corona, $f_c = \rho h u^2$. (*d–f*) The time evolution of the dimensionless (*d*) corona radius $R = r/r_1$, (*e*) radial speed $U = u/u_1$ and (*f*) edge thickness $H = h/r_1$ for different Weber numbers. Here, $T = t/\tau$ is the dimensionless time, with impact time $\tau = r_1/u_1$.

the impacting drop expands into a corona. This expansion is decelerated by surface viscous stresses and surface tension. As it decelerates, the force of impact with the sessile drop along the way decreases with the distance of expansion r (figure 7*a*). The impact *We* determines the radial speed of corona expansion $u = \mathrm{d}r/\mathrm{d}t$ in addition to its maximum extension r_{max} (figure 7*b*). The interplay of the corona expansion speed u and the drop–drop offset d determines the force of impact between the corona and the sessile drop. In particular, for a given impact *We*, the larger the interdrop distance d is, the smaller the momentum transfer from the edge of the corona to its neighbouring sessile drop upon impact is.

We can formalize this physical picture further by defining a horizontal collision Weber number We_c characterizing the competition between the inertia of the corona edge and the interfacial forces of the sessile drop. For a given impact *We*, there should exist a critical collision distance, r_c, such that $r_1 + r_2 < d - r_2 < r_c < r_{max}$, below which We_c is high enough for the horizontal collision to impart high enough inertia to the sessile drop to overcome capillarity, transforming the sessile drop into an expanding sheet in the air. For an interdrop distance r_c such that $r_c < d - r_2 < r_{max}$, this would not be the case and only a touch-and-flop collision could occur.

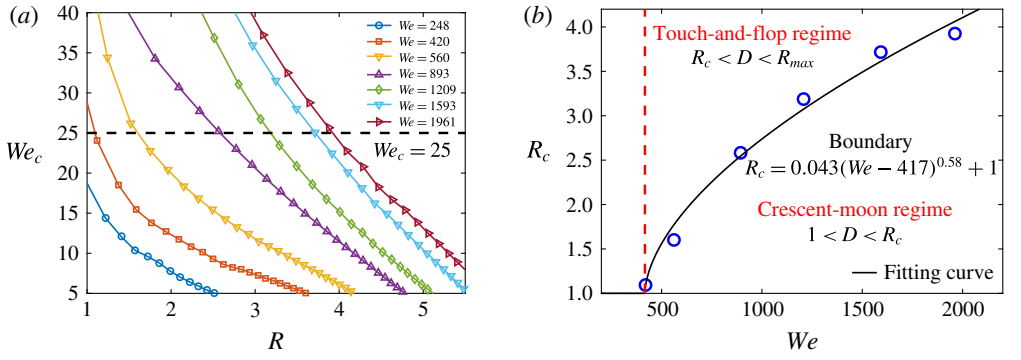

FIGURE 8. (Colour online) (*a*) The collision Weber number We_c as a function of the dimensionless corona radius R. The collision Weber number We_c is the ratio of the rate of change of momentum (collision force) per unit arclength $\rho u^2 h$ and surface tension σ. (*b*) The critical distance above which crescent-moon fragmentation cannot occur, R_c, as a function of the impact We and at which $We_c = 25$. Below the impacting drop $We = 417$, crescent-moon fragmentation cannot occur regardless of the radial drop–drop interdistance.

We quantify this process with an expression for the drop–drop impact force of the corona per unit arclength,

$$f_c = \rho h u^2, \tag{3.4}$$

where h and u are the thickness and velocity of the corona edge respectively (figure 7*a–c*). This force allows us to derive an expression for the impact horizontal Weber number,

$$We_c = \frac{f_c}{\sigma} = \frac{\rho h u^2}{\sigma}. \tag{3.5}$$

By analogy with impacts normal to a surface, we expect We_c of the order of 1–10 or lower not to allow for sufficient force to transform the sessile drop into a sheet, thus restricting the drop–drop impact outcome to a touch-and-flop. Similarly, we expect values of We_c higher than order 10 to enable crescent-moon sheet formation. We test this expectation in the next section.

3.3.2. *Quantification of threshold impact force from spatiotemporal corona expansion*

Combining top and side analysis of the spatiotemporal corona expansion with detailed calibration of thickness and feature extraction as illustrated in figure 7(*a–c*) (Wang & Bourouiba 2017), we measured the following: the time evolution of the corona area A and its radius $r = \sqrt{A/\pi}$, its edge radial velocity $u = \mathrm{d}r/\mathrm{d}t$ and its average thickness h. The results are shown in figure 7(*d–f*) for a range of impact We. From these results, we can deduce the dependence of the horizontal collision Weber number We_c on the corona radius $R = r/r_1$, as shown in figure 8(*a*), and compute the threshold corona radius r_c above which We_c is too small to induce crescent-moon sheet formation (figure 8*b*). We find that the corresponding threshold value for crescent-moon formation is $We_c = \rho h u^2/\sigma = 25$, associated with a local drop–drop threshold collision force $f_c = 1.2$ kg s^{-2} per unit arclength. It should be noted that $We_c = 25$ is consistent with our expectation of a threshold Weber number of the order of 1–10 by analogy with the classical splash of isolated drops upon impact normal to a solid surface (Yarin 2006; Josserand & Thoroddsen 2016). However,

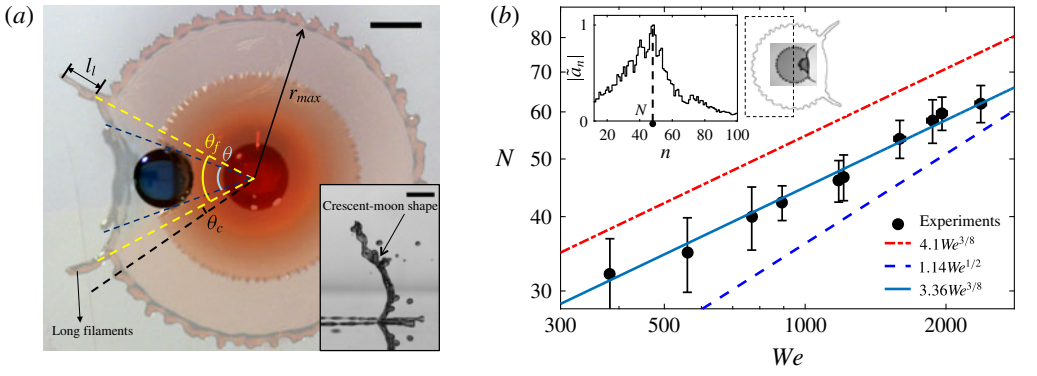

FIGURE 9. (Colour online) (*a*) Overlay of bottom views of the crescent-moon collision, where the opening angle evolves from (4.1) at initial contact between the red corona and the blue sessile drop to (4.3) at maximum corona radius (r_{max}). The scale bar is 4 mm. The corrugation angle of the corona rim is $\theta_c = (\theta_f - \theta)/2$. (*b*) Comparison between the measured and predicted number of corrugations N from the literature: $N = 4.1We^{3/8}$ is the scaling from Marmanis & Thoroddsen (1996) and $N = 1.14We^{1/2}$ is from Mehdizadeh *et al.* (2004); $N = 3.36We^{3/8}$ is the best fit of the experimental data of the present study. The left inset shows the normalized power spectrum of rim corrugations at the maximum corona radius (right inset) as a function of wavenumber. The wavenumber with the peak of the spectrum gives the number of ligaments N.

here, as the drop–drop collision is tangential to a solid surface, we expect more dissipation from tangential surface friction and longitudinal wave propagation in the sessile drop; hence, the critical $We_c = 25$ for the tangential on-surface drop–drop collision is slightly higher compared with normal single drop impacts $We = 1$–10. Figure 8(*a*) also shows that no crescent-moon can occur if We is too small ($We < 417$ here), regardless of the drop–drop interdistance. In summary, the boundary between crescent-moon and touch-and-flop regimes is for

$$1 < D = R_c = 0.043(We - 417)^{0.58} + 1 < R_{max}, \tag{3.6}$$

where $R_c = r_c/r_1$. This expression when overlaid on the D–We regime map of figure 6 is in very good agreement with the data, hence supporting the physical picture of drop–drop impact presented in this section.

4. Crescent-moon: universality of opening angle

To better understand crescent-moon fragmentation, we now turn to the factors governing its features. At impacting drop maximum corona radius r_{max}, the base of the sheet of the crescent-moon is prescribed by an opening angle θ_f and is surrounded by two ligaments of length l_l (figure 9*a*). The values of θ_f and l_l can depend on a range of parameters d, r_1, r_2, u_1, r_{max}, f_c of this complex problem (see figures 2 and 9*a*).

We first elucidate the crescent-moon angle θ_f via a geometrical relation between the falling drop of size r_1 at a distance d from the sessile drop of size r_2. The view from below in figure 9(*a*) shows θ, the angle between the two tangent lines to the sessile

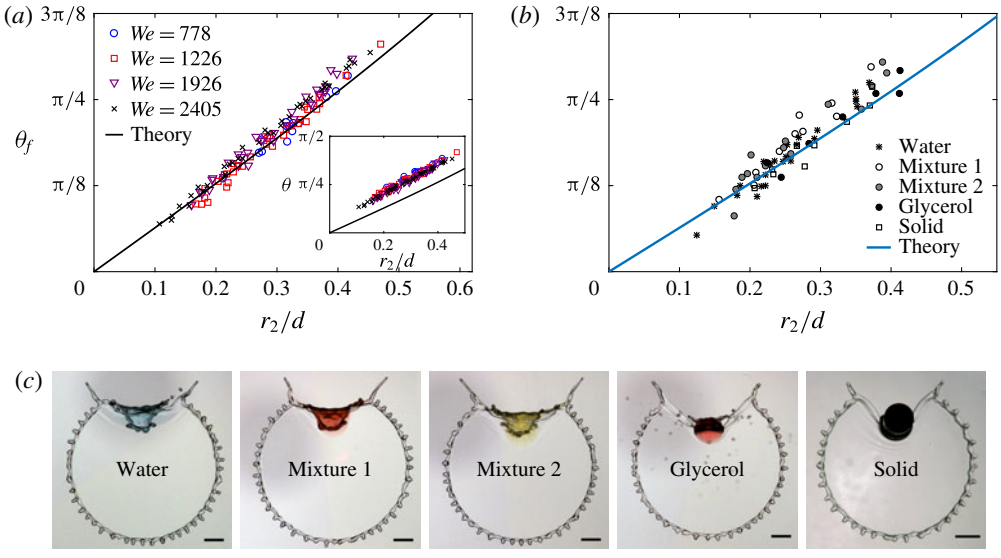

FIGURE 10. (Colour online) (*a*) The match between prediction (4.1)–(4.3) and measurement of crescent-moon opening angle θ_f as a function of r_2/d. (*b*) Robustness of the prediction to increase of sessile drop fluid viscosity and for impact with a solid analogue sessile drop. (*c*) Bottom views of the crescent-moon with sessile drops of increasing viscosity (left to right) and a solid (rightmost), showing the robustness and universality of θ_f and the emerging pair of ligaments. The scale bar is 4 mm.

drop (r_2) originating from the centre of the impacting drop at radial distance d. Simple geometry yields

$$\theta = 2 \arcsin\left(\frac{r_2}{d}\right). \tag{4.1}$$

The inset to figure 10(*a*) compares the predicted opening angle θ (4.1) and its measurement θ_f as in figure 9(*a*). The prediction and observation differ by a systematic bias. We elucidate this bias by closer inspection of the corona of the impacting drop. Prior studies have documented the appearance of corrugations surrounding the expanding coronas of isolated impacting drops on solids, as summarized in table 2. We observe that during corona expansion, the angle θ (4.1) defining the base of the crescent-moon sheet is stretched outward (figure 9*a*). The fluid accumulated in the flaps surrounding the sessile drop settles and is entrained and absorbed into the two closest corrugations of the corona rim. This process is further discussed in § 5.

To elucidate the systematic bias of the prediction of the opening angle in figure 10(*a* inset), we analyse the average angle θ_c between rim corrugations at maximum corona radius r_{max}, $\theta_c = 2\pi/N$, where N is the total number of rim corrugations (figure 9*b*). To measure the total number of ligaments systematically, we take the Fourier transform of the rim corrugations, leading to a power spectrum as a function of the wavenumber $n = 2\pi r_{max}/\lambda_n$ (figure 9*b* inset), where λ_n is the wavelength. We use the dominant mode (wavenumber corresponding to the peak of the spectrum) as the number of ligaments N. Correction of the prediction (4.1) by the obtained intercorrugation angle $\theta_c = 2\pi/N$ leads to figure 10(*a*). The opening angle predicted, $\theta + 2\theta_c$, and that measured match very well.

In addition, our Fourier analysis shows that the number of rim corrugations N at maximum corona radius is well captured by

$$N = C_N\, We^{3/8}, \tag{4.2}$$

with $C_N = 3.36$ as seen in figure 9(*b*). Equation (4.2) falls between prior scalings proposed in the literature (§ 1.2 and table 2) and matches the empirical expression proposed by Marmanis & Thoroddsen (1996) particularly well. We expect C_N to be sensitive to surface roughness, wetting and temperature. The value of $C_N = 3.36$ obtained in this paper was, however, robust to the range of contact angles of average wetting of interest herein, $45° \leqslant \theta_e \leqslant 82°$ (discussed thereafter in figure 12). The value of $C_N = 3.36$ is fixed for the remainder of the study.

Hence, we can predict the opening angle of the crescent-moon, θ_f, completely from the geometric parameters d and r_2 and the dynamic parameter We as

$$\theta_f = 2\arcsin\left(\frac{r_2}{d}\right) + \frac{4\pi}{C_N We^{3/8}}, \tag{4.3}$$

with $C_N = 3.36$ fixed, which is robust to change of the impact Weber number, as shown in figure 10(*a*). To investigate further the robustness of the prediction, we conducted an extensive series of experiments where the sessile drop was changed from inviscid to viscous, to a solid drop-analogue with similar size and geometry to the sessile drop as seen from below in figure 10(*c*) (see table 4 for the fluids and solids used). We found that the prediction of θ_f (4.3) is robust to change of sessile fluid properties and is even robust for impacts of expanding coronas on sessile solids, as shown in figure 10(*b*,*c*). This robust match confirms that crescent-moon fragmentation is governed by geometry at first order and governed by dynamics, via impacting drop corona destabilization, at second order.

5. Crescent-moon: universality of ligament length

We now turn to the length of the ligaments, l_l (figure 11*a*). Upon impact with the sessile drop, the impacting drop corona is obstructed. Close observation reveals that the fluid in the crescent-moon sheet is from the sessile drop, while the fluid in the ligaments surrounding its base is from the impacting drop corona (figures 2*c*, 3*c*, 9*a* and 10*c*). We conducted an extensive set of experiments and predicted the length l_l of the two ligaments bounding the crescent-moon (figure 10*c*).

Careful observation (e.g. figure 11*a* inset) reveals that the fluid of the obstructed corona (pink in figure 11*a*) is diverted as it flows out along the sides of the lifted sessile drop (blue in figure 11*a*), where the sessile drop and the expanding drop sheet connect. The two regions, or flaps, surrounding the sessile drop (blue shadowed flaps in figure 11*a*) are initially formed around the sessile drop sheet suspended in the air (e.g. figure 11*b* inset). When the corona sheet reaches maximum radius r_{max}, the fluid settles down on the surface and flows radially outward in the corona sheet. On reaching and entering the rim, the fluid is reoriented to flow along the rim, reaching and feeding the closest corrugation. The two surrounding rim corrugations of thickness w_c indeed grow into crescent-moon ligaments of length l_l as a result. We report that the thickness of the two ligaments is similar to that of the rim corrugations,

$$w_c = \frac{2\pi r_{max}}{2N} = \frac{\pi r_{max}}{N}, \tag{5.1}$$

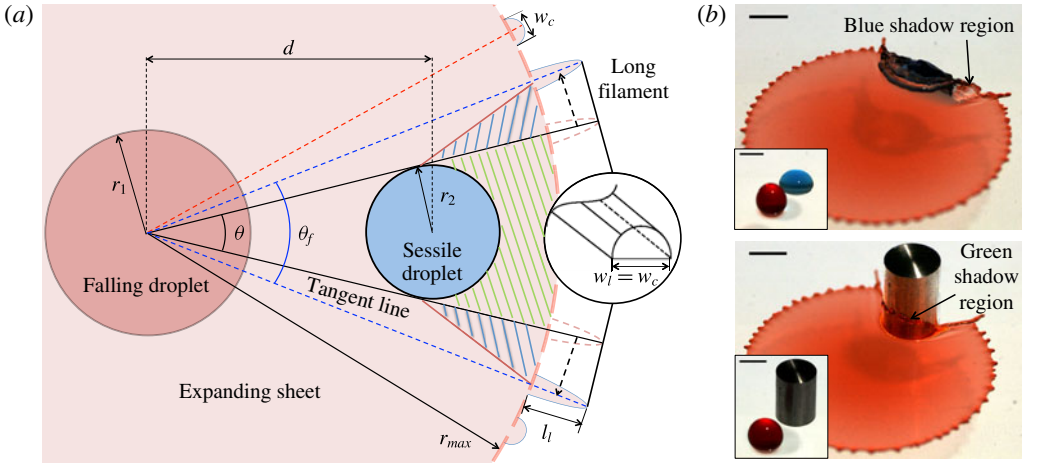

FIGURE 11. (Colour online) (*a*) The impacting drop (dark red) of maximum corona radius r_{max} (light red) with rim corrugations of width w_c is shown with a sessile drop (blue) of radius r_2 at distance d and the crescent-moon pair of cylindrical ligaments of length l_l and width w_c. The fluid in the flaps surrounding the crescent-moon sheet (blue shadow region) is originally lifted up. (*b*) Impact of an expanding corona on a sessile drop (upper panel) and a solid drop-analogue (lower panel). At corona radius r_{max}, the fluid in the flaps settles and feeds the pair of ligaments. The scale bar is 4 mm.

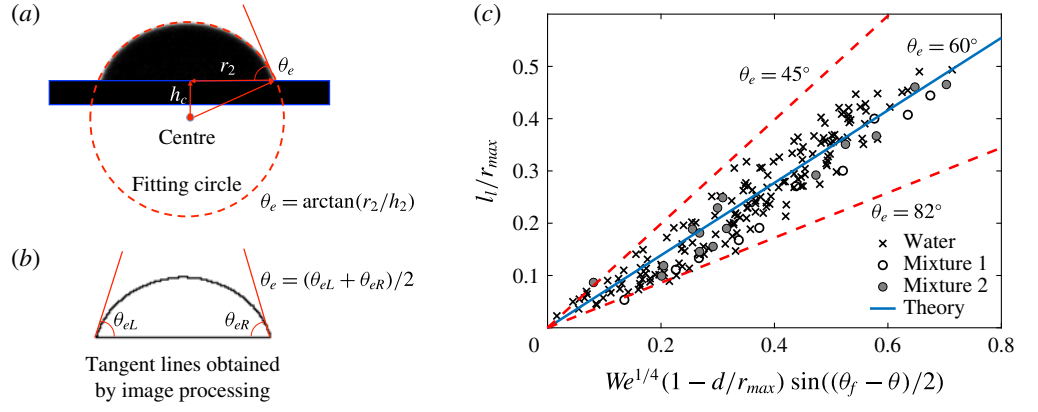

FIGURE 12. (Colour online) (*a*) Side view of a sessile drop on a solid surface. A circle is fitted to the drop. The contact angle is measured on both sides and averaged such that $\theta_e = \arctan(r_2/h_c)$, where r_2 is the radius of the base of the sessile drop and h_c is the distance between the surface plane and the centre of the circle. (*b*) The contour of the sessile drop in (*a*) detected using an image processing algorithm. (*c*) The agreement between our prediction of ligament length (5.8) at maximum corona radius and our experimental data.

as shown in figures 9(*a*) and 11(*b*). Based on this physical picture, the resulting volume of fluid expected to be in the two flaps in the air surrounding the crescent-moon sheet should be equal to the volume of the two bounding ligaments.

From geometry (figure 11*a* shadowed blue regions), the volume of fluid in the flaps surrounding the crescent-moon sheet is

$$V_s = A_s h, \tag{5.2}$$

where h is the average thickness of the corona at maximum radius and A_s is the area of the flaps, which can be expressed by

$$A_s \approx (r_{max} - d) r_{max} \sin\left(\frac{\theta_f - \theta}{2}\right). \tag{5.3}$$

At maximum corona radius r_{max}, the average corona thickness is

$$h = V/\pi r_{max}^2 = \frac{4}{3} r_1^3 / r_{max}^2, \tag{5.4}$$

with $V = (4/3)\pi r_1^3$ the initial impacting drop volume.

The volume of the ligaments (figure 11*a*) is

$$V_f = 2 A_f l_l, \tag{5.5}$$

with cross-sectional area $A_f = C_s w_c^2$, by assuming their shape to be semicylindrical of width w_c, as shown in figure 11(*a*). The geometrical coefficient C_s can be expressed as

$$C_s = \tfrac{1}{4}(\theta_e \csc^2 \theta_e - \cot \theta_e), \tag{5.6}$$

where θ_e is the equilibrium contact angle of the fluid on the surface. We measured the contact angle using image processing on the two sides of the sessile drops as shown in figure 12(*a*,*b*). Our measurements give a mean contact angle of $\theta_e = 60°$, and thus $C_s = 0.2047$, with a maximum angle of 82° and a minimum angle of 45°.

By equating the volume of the flaps V_s to the volume of the ligaments V_l, we obtain a prediction for the length of the ligaments as

$$\frac{l_l}{r_{max}} = \frac{2}{3C_s}\left(\frac{N}{\pi}\right)^2 \left(\frac{r_1}{r_{max}}\right)^3 \left(1 - \frac{d}{r_{max}}\right) \sin\left[\frac{\theta_f - \theta}{2}\right]. \tag{5.7}$$

It should be recalled that we have already determined and fixed the constants associated with the dimensionless maximum corona radius $R_{max} = r_{max}/r_1$ in (3.3) (figure 5) and the number of corrugations, N, of the corona at its maximum radius R_{max} in (4.2) (figure 9*b* and § 4). By leveraging these prior findings, the ligament length predicted is

$$\frac{l_l}{r_{max}} = C_L We^{1/4} \left(1 - \frac{d}{r_{max}}\right) \sin\left[\frac{\theta_f - \theta}{2}\right] \tag{5.8}$$

or

$$\frac{l_l}{r_1} = C_R C_L We^{5/12} \left(1 - \frac{d}{r_1 C_R} We^{-1/6}\right) \sin\left[\underbrace{\frac{2\pi}{C_N}}_{\approx 2} We^{-3/8}\right], \tag{5.9}$$

in terms of initial impact parameters. The constants are interdependent, with

$$C_L = \frac{2}{3\pi^2 C_s}\left(\frac{C_N^2}{C_R^3}\right), \tag{5.10}$$

where all constants are fixed by our prior measurements (no free parameter) and given by (5.6), (3.3) and (4.2) with $C_L = 0.69$ for $C_s = 0.2047$, $C_R = 1.75$ and $C_N = 3.36$. Figure 12(*c*) shows the very good agreement between our prediction (5.8) and our experimental measurements. The dashed lines show the prediction of the length of ligaments corresponding to the minimum and maximum values of contact angle measured (figure 12*a*,*b*). Our data fall within our range of prediction (5.8).

Interestingly, the size of the sessile drop, r_2, does not prescribe the length of the crescent-moon ligaments. Returning to the schematic in figure 11(*a*), one can see that, regardless of r_2, the flap regions of corona fluid forming the ligaments are indeed independent of r_2. They depend directly on the corona extension r_{max} (fixed by r_1 and impact *We*), its corrugation wavelength $\lambda = 2\pi r_{max}/N$ and the interdrop distance d. Prediction (5.8) is robust to increase of sessile drop viscosity up to approximately 30 times that of water (figures 12*c* and 10*c*). The lengths of the ligaments for impacts on solid sessile objects and sessile drops of viscosity 1400 times that of water (i.e. pure glycerol) differ however. This is expected given that (5.8) is based on the key observation that the ligaments are formed of the fluid of the lifted flaps surrounding the deformed sessile drop (figure 11*a*,*b*). The lift of the sessile drop and formation of flaps continues to be the dominant feature of the crescent-moon regime for sessile drop viscosities of up to 30 times that of water (mixtures 1 and 2 in figure 10*c* and table 4), but can no longer occur for pure glycerol and rigid objects. In addition, one of the underlying assumptions of our model is that both interacting drops have comparable sizes (as found in sprays and rainfalls), and both are assumed to be of the order of or smaller than the capillary length. By construction, equation (5.9) is established for the crescent-moon *We*–*D* regime (figure 6). Finally, one last underlying assumption is that the corona corrugation wavelength is smaller than the typical sessile drop size considered: $\lambda < r_2$. This last assumption is clearly always true for the water drops of interest for sprays and rainfalls motivating the present study.

6. Conclusion

Drop impacts on surfaces are ubiquitous in agriculture, coating and pathogen transport. Most extensive research on drop impacts has focused on idealized superhydrophobic or fully wetting surfaces. Despite the ubiquity of surfaces of intermediate wetting (not fully wetting or superhydrophobic) in nature, indoors and in industry, little is understood about the physics of impacts on them. Combining experiments and modelling, we show that such surfaces, which support sessile drops, lead to dramatically different regimes of coating and splash from those inferred from isolated impacts. We showed that four regimes of drop–drop interaction emerge: *head-on collision*, *crescent-moon fragmentation*, *touch-and-flop collision* and *no collision* (figures 3 and 6). These regimes include novel fragmentation phenomena only recently identified as ubiquitous in impacts on plant surfaces (Gilet & Bourouiba 2015), such as the *crescent-moon fragmentation*. Herein, we have predicted the transitions between these four regimes accurately based on two dimensionless parameters: the impacting drop Weber number and the normalized interdistance between the two drops (figure 6). We have shown that a critical drop–drop impact

force governs the existence and physics of the crescent-moon fragmentation and that this force is shaped by a subtle combination of geometry and momentum transfer. We introduced a horizontal critical collision Weber number We_c below which crescent-moon fragmentation cannot occur. The horizontal critical collision Weber number We_c is defined based on the force per unit length upon collision of the rim of the expanding corona onto the sessile drop. Below $We_c = 25$, the momentum imparted to the sessile drop is not sufficient to transform its bulk into an expanding sheet characteristic of a crescent-moon. Using the geometric constraint of the drop–drop interaction and volume conservation, we also predicted and validated the models governing two peculiar features of crescent-moon fragmentation: the width of the base of its expanding sheet in the air and the length of the pair of ligaments surrounding its base. We showed that the predictions of these two properties are robust to a wide range of surface average wettings and sessile drop fluid viscosities. Prediction of these properties is important for the study of crescent-moon fragmentation, which is a highly efficient producer of secondary droplets.

Our findings bring a fundamental understanding to a ubiquitous, yet so far neglected, drop–drop interaction physical phenomena. Our results suggest a new paradigm: impacts on most surfaces can make a splash of a new kind – a crescent-moon – for any impact velocity when neighbouring sessile drops are present. Hence, interactions between sessile and impacting drops of comparable sizes can alter the washing and coating of surfaces significantly, while increasing spray drift or rain-induced pathogen transmission from contaminated surfaces in agriculture. Elucidation of the final stages of drop–drop impact fragmentation in this agricultural context is our current focus.

Acknowledgements

This research was partially supported by NSF CBET-1546990 and the USDA-NIFA Specialty Crop Research Initiative Grant Award No. MDW-2016-04938. Y.W. is grateful for the partial support of the MIT J. S. Hennessy ODGE Fellowship.

REFERENCES

BARNES, H. A., HARDALUPAS, Y., TAYLOR, A. & WILKINS, J. H. 1999 An investigation of the interaction between two adjacent impinging droplets. In *Proceedings of the 15th International Conference on Liquid Atomisation and Spray Systems (ILASS), Toulouse*, pp. 1–7. ONERA.

BHOLA, R. & CHANDRA, S. 1999 Parameters controlling solidification of molten wax droplets falling on a solid surface. *J. Mater. Sci.* **34** (19), 4883–4894.

BOUROUIBA, L. & BUSH, J. W. M. 2013 Drops and bubbles in the environment. In *Handbook of Environmental Fluid Dynamics* (ed. H. J. S. Fernando), chap. 32, pp. 427–439. Taylor and Francis Book Inc.

BOUROUIBA, L., DEHANDSCHOEWERCKER, E. & BUSH, J. W. M. 2014 Violent expiratory events: on coughing and sneezing. *J. Fluid Mech.* **745**, 537–563.

CHANDRA, S. & AVEDISIAN, C. T. 1991 On the collision of a droplet with a solid surface. *Proc. R. Soc. Lond.* A **432**, 13–41.

CHARALAMPOUS, G. & HARDALUPAS, Y. 2016 Impingement and splashing of droplets on spherical targets. In *54th AIAA Aerospace Sciences Meeting (AIAA 2016-1448)*, pp. 1–12. AIAA.

CLANET, C., BÉGUIN, C., RICHARD, D. & QUÉRÉ, D. 2004 Maximal deformation of an impacting drop. *J. Fluid Mech.* **517**, 199–208.

EGGERS, J., FONTELOS, M. A., JOSSERAND, C. & ZALESKI, S. 2010 Drop dynamics after impact on a solid wall: theory and simulations. *Phys. Fluids* **22**, 1–13.

EGGERS, J. & VILLERMAUX, E. 2008 Physics of liquid jets. *Rep. Prog. Phys.* **71**, 036601.

FUJIMOTO, H., ITO, S. & TAKEZAKI, I. 2002 Experimental study of successive collision of two water droplets with a solid. *Exp. Fluids* **33**, 500–502.

FURBISH, D. J., HAMMER, K. K., SCHMEECKLE, M., BOROSUND, M. N. & MUDD, S. M. 2007 Rain splash of dry sand revealed by high-speed imaging and sticky paper splash targets. *J. Geophys. Res. Earth Surf.* **112**, 1–19.

GILET, T. & BOUROUIBA, L. 2014 Rain-induced ejection of pathogens from leaves: revisiting the hypothesis of splash-on-film using high-speed visualization. *Integr. Compar. Biol.* **54**, 974–984.

GILET, T. & BOUROUIBA, L. 2015 Fluid fragmentation shapes rain-induced foliar disease transmission. *J. R. Soc. Interface* **12**, 20141092.

JOSSERAND, C. & THORODDSEN, S. T. 2016 Drop impact on a solid surface. *Annu. Rev. Fluid Mech.* **48**, 365–391.

LAAN, N., DE BRUIN, K. G., BARTOLO, D., JOSSERAND, C. & BONN, D. 2014 Maximum diameter of impacting liquid droplets. *Phys. Rev. Appl.* **2**, 1–7.

LASTAKOWSKI, H., BOYER, F., BIANCE, A. L., PIRAT, C. & YBERT, C. 2014 Bridging local to global dynamics of drop impact onto solid substrates. *J. Fluid Mech.* **747**, 103–118.

LEE, J. B., DEROME, D., DOLATABADI, A. & CARMELIET, J. 2016 Energy budget of liquid drop impact at maximum spreading: numerical simulations and experiments. *Langmuir* **32**, 1279–1288.

LIANG, G. & MUDAWAR, I. 2016 Review of mass and momentum interactions during drop impact on a liquid film. *Intl J. Heat Mass Transfer* **101**, 577–599.

MADEJSKI, J. 1976 Solidification of droplets on a cold surface. *Intl J. Heat Mass Transfer* **19**, 1009–1013.

MARMANIS, H. & THORODDSEN, S. T. 1996 Scaling of the fingering pattern of an impacting drop. *Phys. Fluids* **10**, 1344–1346.

MEHDIZADEH, N. Z., CHANDRA, S. & MOSTAGHIMI, J. 2004 Formation of fingers around the edges of a drop hitting a metal plate with high velocity. *J. Fluid Mech.* **510**, 353–373.

MOREIRA, A. L. N., MOITA, A. S. & PANÃO, M. R. 2010 Advances and challenges in explaining fuel spray impingement: how much of single droplet impact research is useful? *Prog. Energy Combust. Sci.* **36**, 554–580.

RIOBOO, R., MARENGO, M. & TROPEA, C. 2002 Time evolution of liquid drop impact onto solid, dry surfaces. *Exp. Fluids* **33**, 112–124.

SCHARFMAN, B. E., TECHET, A. H., BUSH, J. W. M. & BOUROUIBA, L. 2016 Visualization of sneeze ejecta: steps of fluid fragmentation leading to respiratory droplets. *Exp. Fluids* **57**, 24.

SCHELLER, B. L. & BOUSFIELD, D. W. 1995 Newtonian drop impact with a solid surface. *AIChE J.* **41**, 1357–1367.

SIVAKUMAR, D. & TROPEA, C. 2002 Splashing impact of a spray onto a liquid film. *Phys. Fluids* **14**, 10–14.

WANG, Y. & BOUROUIBA, L. 2017 Drop impact on solid: unified thickness profile of the expanding sheet in the air. *J. Fluid Mech.* **814**, 510–534.

YARIN, A. L. 2006 Drop impact dynamics: splashing, spreading, receding, bouncing . . . . *Annu. Rev. Fluid Mech.* **38**, 159–192.

YARIN, L. & WEISS, D. 1995 Impact of drops on solid surfaces: self-similar capillary waves, and splashing as a new type of kinematic discontinuity. *J. Fluid Mech.* **283**, 141–173.

ZABLE, J. L. 1977 Splatter during ink jet printing. *IBM J. Res. Dev.* **21**, 315–320.